Journal of Solid Mechanics Vol. 14, No. 2 (2022) pp. 252-271
DOI: 10.22034/jsm.2021.1942740.1718

New Two 20-Node High-Order Finite Elements Based on the SFR Concept for Analyzing 3D Elasticity Problems

H. Djahara [1,*] , K. Meftah [1,3], L. Sedira [2], A. Ayadi [1]

[1] *Laboratoire de Génie Energétique et Matériaux (LGEM), University of Biskra, Biskra, Algeria*
[2] *Laboratoire de Génie Mécanique (LGM), University of Biskra, Biskra, Algeria*
[3] *University of Batna 2, Faculty of Technology, Department of Mechanics, Batna, Algeria*

Received 24 February 2022; accepted 20 April 2022

ABSTRACT

This paper proposes conforming and nonconforming 20-node hexahedral finite elements. The elements' formulation stems from the so-called Space Fiber Rotation (SFR) concept, allowing a spatial rotation of three-dimensional virtual fiber within the elements. Adding rotational degrees of freedom results in six degrees of freedom per node (three rotations and three translations) which enhances the approximation of the classical displacement field. The incompatible modes approach has been adopted in the nonconforming element formulation in order to avoid numerical deficiencies associated with the Poisson's ratio locking phenomenon. The accuracy of the proposed elements is examined through a series of three-dimensions linear elastic benchmarks including beam, plates, and shell structures. The proposed elements were shown to give better results than the standard 20-node hexahedron especially when mesh distortion is applied. This confirms that the two proposed elements are less sensitive to mesh distortion. The elements also show good performance when compared with analytical and numerical solutions from the literature.

Keywords : 3D finite element; 20-node hexahedron; Space fiber rotation; High order formulation; Incompatible modes method.

1 INTRODUCTION

THE finite element method (FEM) is considered one of the most powerful tools in numerical simulation owing to its reliability, robustness, and efficiency. Since the first mathematical proofs on its formulation Babuska and Aziz [1], the FEM has emerged as powerful platform for solving PDEs in a range of fields such as heat transfer, fluid mechanics, electromagnetic potential, and even in the development of efficient nanoscale systems [2]. In solid mechanics, 3D modeling has been attracting a lot of interest especially with the enormous growth of computational resources. The element formulation plays a crucial role in finite element analysis (FEA). Since its early days, many attempts have been made to enhance the performance of finite elements in a matter of accuracy, efficiency, and versatility. This resulted in a plethora of models and approaches where many pioneering works have been published and ended up being integrated into commercial finite element software. To meet the requirement of 3D modeling,

---

[*] Corresponding author. Tel.: +213 0698 870 905.
E-mail address: hossam.djahara@univ-biskra.dz (H. Djahara)

the development of low order solid elements with high performance has gained great importance. Standard low order hexahedral elements were very beneficial in terms of computational cost. However, these elements suffer from some well-known deficiencies under some circumstances. For example, locking, a phenomenon that generally occurs when shape functions fail to interpolate a field correctly [3], may lead results. Hughes et al. [4] and Zienkiewcs et al. [5] successfully overcame locking phenomena by introducing the reduced and selective reduced integration techniques, respectively. Wilson et al. [6] introduced incompatible displacement modes to enhance the displacement field of the element. As this approach was just limited to parallelograms, Taylor et al. [7] adjusted this formulation by correcting the defective terms and examining the patch test. Working along similar lines, Simo and Rifai [8] developed a family of three elements based on the approach of Enhanced Assumed Strain (EAS), a method that considers adding an extra field of variables to the strain field, to account for linear problems. Similarly, Andelfinger and Ramm [9] used the EAS concept to develop membrane, plate and shell finite elements where the equivalence with Hellinger-Reissner (HR) elements was discussed. Associated with the Hu-Washizu principle, this EAS technique was implemented to account for the nonlinear regime in the work of Simo and Armero [10] as well as in the work of Simo et al. [11]. On the other hand, several 3D finite elements were also developed based on this technique. This includes the work of Fredriksson and Ottosen [12] in which a stabilized hexahedral element was presented and evaluated through 3D elasticity problems. In the same vein, Sousa et al. [13] presented a class of solid finite elements that is less sensitive to mesh distortion, this resulted in high accuracy in 3D and thin shell applications. Another approach that has been suggested in the literature in order to produce highly accurate finite elements is the hybrid/mixed formulations [14]. Hybrid elements are essentially based on the enforcement of the constraint conditions to ensure interelement compatibility by introducing Lagrange multipliers [15] whereas Mixed elements are derived from a multifield variational functional. Many other pioneering works have been also proposed in this context for linear and nonlinear analysis [16, 17, 18, 19, 20], to name but a few. Moreover, finite elements possessing rotational degrees of freedom were shown to be very efficient in and nonlinear structural problems. Since the inspiring work of Allman [21], numerous successful approaches to embody rotational DOFs in 2D and 3D finite elements have been presented [22, 23, 24, 25]. Yunus et al. [22] used the Hybrid formulation to develop hexahedral, quadrilateral, and triangular finite elements for solving 3D and 2D elasticity problems. In the same perspective, a hexahedron and a tetrahedron finite element were developed in the works of Yunus et al. [23] and Pawlak et al. [24]. The rotational DOFs in these elements were the result of the transformation of the mid-side translational DOF of the standard 20-node hexahedron and 10-node tetrahedron, respectively. Recently, Shang et al. [26] presented an 8-node hexahedral element to analyze size-dependent problems. The 48-DOF element stems from an earlier formulation Shang et al. [27] which is essentially based on the modified couple stress theory. Another pioneering attempt to produce high accurate finite elements with rotational DOF is the Space Fiber Rotation (SFR) concept. This approach, firstly introduced by Ayad [25], considers the rotation of a spatial virtual fiber within the element which results in additional rotational DOFs. This assumption has been adopted by several authors [28, 29, 30, 31, 32, 33, 34] to develop a family of efficient 2D and 3D finite elements. In his innovative work, Ayad et al. [29] presented two 8-node hexahedrons: conforming (SFR8) and nonconforming (SFR8I) finite elements. The later includes three incompatible modes and was mainly proposed to overcome the Poison's ratio locking problem present within the SFR8 element. These elements were adopted in the paper of Meftah et al. [30] to account for geometrical nonlinear problems. In the same regard, a multilayer version of the SFR8 element, called SFR8M, was introduced by Meftah et al. [31] to model composite laminated structures. Meftah and Sedira [32] suggested a linear four-node tetrahedral finite element SFR4 for modeling solid structures. Recently, Ayadi et al. [33] adopted the SFR approach to analyze 3D nonlinear elastoplastic problems. High order finite element has also gained a renewed interest especially with the massive development of computational resources. This was motivated by the fast convergence and high accuracy of these elements. Over the past few years, numerous 2D finite elements have been published in this context [35, 36, 37], to cite but a few. On the other hand, some high order solid finite element has been proposed for 3D modeling. Ooi et al. [38] suggested a 20-node hexahedron based on an asymmetric that exploits intrinsic properties of different sets of shape functions. This resulted in an efficient finite element with high tolerance to mesh distortion. This approach was later extended to include geometric nonlinearities [39]. Li et al. [40] presented a 21-node hexahedral spline element that incorporates an internal node and reaches the second order completeness of Cartesian coordinates. The element was shown to be better than the standard 20-node serendipity elements especially in terms of sensitivity to mesh distortion.

The paper presents new two high order hexahedral finite elements named SFR20 and SFR20I for solving 3D elastic problems. The 20-node elements belong to the family of SFR finite elements which, as previously stated, considers the spatial rotation of a virtual fiber within the element resulting in an enhancement in the displacement vector approximation. This work is an extension to a previous work by Ayad et al. [29]. The main contribution is to increasing the order of shape functions for the displacement fields in order to increase the performance of the element and can be insensitive to particular types of mesh distortion. The SFR20I is a nonconforming version of the SFR20 element which is mainly proposed to avoid numerical difficulties related to Poisson's ration locking phenomena. The remaining part of the paper proceeds as follows: Section 2 presents the variational finite element formulation. Section 3 and 4 are concerned with the formulation of the two proposed elements. The numerical integration scheme used to obtain the element's stiffness matrix is presented in section 5. In order to evaluate the performance of the proposed elements, several numerical examples with different geometries are examined in section 6. Some concluding remarks are outlined in the seventh and last section.

2 VARIATIONAL FINITE ELEMENT FORMULATION

The equilibrium of the solid body depicted in Fig. 1 can be defined as:

$$\iint_s \vec{T}dS + \iiint_V \vec{f}dV = 0 \tag{1}$$

Calling Ω the continuous domain bounded by boundary Γ, where the first term represents the action of all surface forces and the second represents the action of all forces of volume. The boundary of Ω is split into Γ_u and Γ_σ, so that $\Gamma = \Gamma_u \cup \Gamma_\sigma$ and $\Gamma_u \cap \Gamma_\sigma = \varnothing$. Based on these notations, the boundary conditions are expressed as:

$$\begin{cases} U_i = U_i^* & on \quad \Gamma_u \\ \sigma_{ij} n_j = T_i & on \quad \Gamma_\sigma \end{cases} \tag{2}$$

where $\underline{T}$ and $\underline{U}^*$ are the prescribed boundary values of traction and displacement, respectively, and n_i is the i^{th} component of the normal vector, and $\underline{U}$ is the displacement vector of Ω.

Using the divergence theorem, Eq. (1) can be rewritten:

$$div\left(\underline{\underline{\sigma}}\right) + \underline{f}^v = 0 \quad in \quad \Omega \tag{3}$$

where $\underline{\underline{\sigma}}$ and $\underline{f}^v$ are respectively the mechanical stress tensor and the body force.

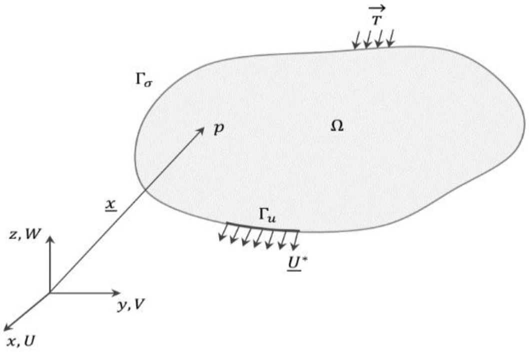

Fig.1
Equilibrium of an elastic domain.

The weak form W of the equilibrium Eq. (1) can be obtained by introducing the admissible test function $\delta\underline{U}$ verifying:

$$W = \int_\Omega \delta\underline{U}(div(\underline{\underline{\sigma}}) + \underline{f}^v)d\Omega = 0 \qquad \forall \delta\underline{U} \tag{4}$$

$$W = \int_\Omega \sigma_{ij}\delta\varepsilon_{ij}d\Omega - \left[\int_\Omega f_i^v \delta U_i d\Omega + \int_{\Gamma\sigma} T_i \delta U_i dA\right] = 0 \tag{5}$$

$$\begin{cases} W_{int} = \int_{\Omega} \sigma_{ij}\, \delta\varepsilon_{ij}\, d\Omega \\ W_{ext} = \int_{\Omega} f_i^{\,v}\, \delta U_i\, d\Omega + \int_{\Omega} T_i\, \delta U_i\, dA \\ W = W_{int} + W_{ext} = 0 \end{cases} \tag{6}$$

where δW_{int} and δW_{ext} are respectively the internal and external mechanical virtual works.

The virtual linearized strain tensor $\delta\underline{\underline{\varepsilon}}$ is related to $\delta\underline{U}$ by the following expression:

$$\delta\underline{\underline{\varepsilon}} = \frac{1}{2}\left(\underline{\underline{grad}}\left(\delta\underline{U}\right) + \underline{\underline{grad}}^{T}\left(\delta\underline{U}\right)\right) \tag{7}$$

The weak form (5) can be rewritten in a matrix form as follows:

$$W = \int_{\Omega} \{\delta\varepsilon\}^{T} \{\sigma\} d\Omega - \left[\int_{\Omega} \{\delta U\}^{T} \{f^{v}\} d\Omega + \int_{\Gamma\sigma} \{\delta U\}^{T} \{T\} dA\right] = 0 \tag{8}$$

where σ and ε are respectively the Cartesian stress and strain vectors given by:

$$\begin{cases} \{\sigma\} = \{\sigma_{xx}\, \sigma_{yy}\, \sigma_{zz}\, \sigma_{xy}\, \sigma_{xz}\, \sigma_{yz}\}^{T} \\ \{\varepsilon\} = \{\varepsilon_{xx}\, \varepsilon_{yy}\, \varepsilon_{zz}\, \gamma_{xy}\, \gamma_{xz}\, \gamma_{yz}\}^{T} \end{cases} \tag{9}$$

with $\gamma_{xy} = 2\varepsilon_{xy}$, $\gamma_{xz} = 2\varepsilon_{xz}$, $\gamma_{yz} = 2\varepsilon_{yz}$.

3 KINEMATICS OF THE SPACE FIBER ROTATION CONCEPT

This section describes the kinematics of the proposed finite elements. The 20-node hexahedrons are developed based on the SFR concept. As depicted in Fig. 2 this approach considers 3D rotation of a virtual fiber $\underline{iq}$. The fiber rotation represented by the vector $\underline{\theta}$ results in an additional displacement vector f which contribute to the definition of the final displacement field and can be expressed as:

$$\underline{U}_q = \sum_{i=1}^{n=20}\left[N_i \underline{U}_i + f\left(\underline{\theta}_i, \underline{iq}\right)\right] \tag{10}$$

where $\underline{U}_i = \{U_i V_i W_i\}^{T}$ are the parameters of the nodal displacement and N_i are the shape functions associated with the serendipity 20-node hexahedral element, which can be expressed as:

$$\begin{aligned} N_i(\xi,\eta,\zeta) &= \frac{1}{8}\left(-2 + \xi_i\xi + \eta_i\eta + \zeta_i\zeta\right)\left(1+\xi_i\xi\right)\left(1+\eta_i\eta\right)\left(1+\zeta_i\zeta\right) \quad with \quad i = 1,3,5,7,9,11,13,15,17,19 \\ N_i(\xi,\eta,\zeta) &= \frac{1}{4}\left(1-\xi^2\right)\left(1+\eta_i\eta\right)\left(1+\zeta_i\zeta\right) \quad with \quad i = 2,6,14,18 \\ N_i(\xi,\eta,\zeta) &= \frac{1}{4}\left(1+\xi_i\xi\right)\left(1-\eta^2\right)\left(1+\zeta_i\zeta\right) \quad with \quad i = 4,8,16,20 \\ N_i(\xi,\eta,\zeta) &= \frac{1}{4}\left(1+\xi_i\xi\right)\left(1+\eta_i\eta\right)\left(1-\zeta^2\right) \quad with \quad i = 9,10,11,12 \\ & where \quad -1 \le \xi,\eta,\zeta \le +1 \end{aligned} \tag{11}$$

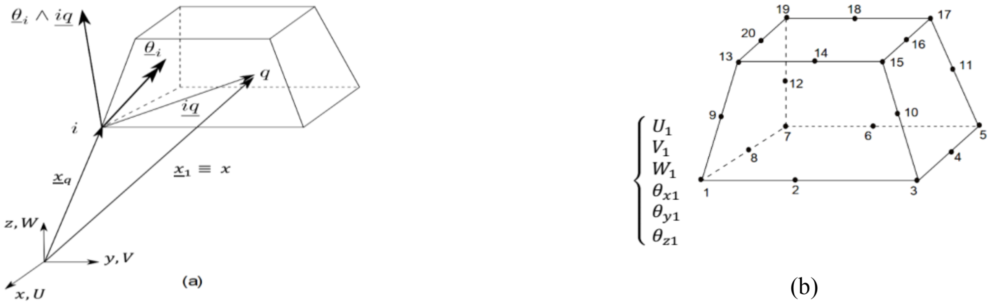

Fig.2
The SFR concept; (a) 3D rotation of the virtual fiber $\underline{iq}$ inducing an additional displacement, (b) the 20-node hexahedral element SFR20 and its nodal variables.

The additional displacement vector is given by:

$$f\left(\underline{\theta}_i,\underline{iq}\right)=N_i\left(\underline{\theta}_i\wedge\underline{iq}\right) \tag{12}$$

where:

$$iq=x_q-x_i=\begin{Bmatrix}x-x_i\\ y-y_i\\ z-z_i\end{Bmatrix}\quad;\quad \theta_i=\begin{Bmatrix}\theta_{xi}\\ \theta_{yi}\\ \theta_{zi}\end{Bmatrix} \tag{13}$$

The global coordinates x,y and z are expressed in terms of nodal coordinates and shape function as:

$$x=\sum_{i=1}^{20}N_i\,x_i\quad;\quad y=\sum_{i=1}^{20}N_i\,y_i\quad;\quad z=\sum_{i=1}^{20}N_i\,z_i \tag{14}$$

Replacing Eq. (13) in Eq. (10) leads to the following improved expression of the displacement field $\underline{U}_q$ of q :

$$\underline{U}\left(\xi,\eta,\zeta\right)=\sum_{i=1}^{20}N_i\left(\xi\;\eta,\zeta\right)\left(\underline{U}_i+\underline{\theta}_i\wedge\underline{iq}\right)\quad;\quad \underline{U}_q\equiv\underline{U} \tag{15}$$

The SFR approximation adopted in Eq. (15) does not affect in any way the inter-element continuity condition of the displacement vector in case where $\underline{iq}$ vanishes when q coincides with the node i . By performing the vector product between the rotation vector $\underline{\theta}_i$ and the virtual fiber $\underline{iq}$, we obtain the following approximation of the displacement vector $\underline{U}$ (the Einstein summation convention on i is used):

$$\{U\}=\begin{Bmatrix}U\\ V\\ W\end{Bmatrix}=\begin{Bmatrix}N_iU_i+N_i\,\left(z-z_i\right)\theta_{yi}-N_i\left(y-y_i\right)\theta_{zi}\\ N_iV_i+N_i\,\left(x-x_i\right)\theta_{zi}-N_i\left(z-z_i\right)\theta_{xi}\\ N_iW_i+N_i\,\left(y-y_i\right)\theta_{xi}-N_i\left(x-x_i\right)\theta_{yi}\end{Bmatrix} \tag{16}$$

The approximation (16) can be expressed in a matrix form:

$$U=\left[N\right]U_n\quad;\quad \left[N\right]=\begin{bmatrix} & \{N_{ui}\}^T & \\ \cdots & \{N_{vi}\}^T & \cdots i=1,20\\ & \{N_{wi}\}^T & \end{bmatrix}=\begin{bmatrix}\{N_u\}^T\\ \{N_v\}^T\\ \{N_w\}^T\end{bmatrix} \tag{17}$$

where:

$$\begin{array}{lclllllll} N_{ui} & = & \{ & N_i & 0 & 0 & 0 & N_i\left(z-z_i\right) & -N_i\left(y-y_i\right) & \}^T \\ N_{vi} & = & \{ & 0 & N_i & 0 & -N_i\left(z-z_i\right) & 0 & N_i\left(x-x_i\right) & \}^T \\ N_{wi} & = & \{ & 0 & 0 & N_i & N_i\left(y-y_i\right) & -N_i\left(x-x_i\right) & 0 & \}^T \end{array} \tag{18}$$

and $\left\{U_n\right\}$ is the nodal DOFs vector containing 6 DOFs (three translations and three rotations) per node.

$$\left\{U_n\right\}=\{\cdots \mid U_i\ V_i\ W_i\ \vdots\ \theta_{xi}\ \theta_{yi}\ \theta_{zi} \mid \cdots i=1,20\}^T \tag{19}$$

From the standard displacement-based finite element functions, the strains of the element can be written as:

$$\varepsilon=\left\{\begin{array}{l}\varepsilon_x \\ \varepsilon_y \\ \varepsilon_z \\ \varepsilon_{xy} \\ \varepsilon_{xz} \\ \varepsilon_{yz}\end{array}\right\}=\left\{\begin{array}{c}\dfrac{\partial u}{\partial x} \\ \dfrac{\partial v}{\partial y} \\ \dfrac{\partial w}{\partial z} \\ \dfrac{\partial u}{\partial y}+\dfrac{\partial v}{\partial x} \\ \dfrac{\partial u}{\partial z}+\dfrac{\partial w}{\partial x} \\ \dfrac{\partial v}{\partial z}+\dfrac{\partial w}{\partial y}\end{array}\right\}=\left[B\right]U_n \tag{20}$$

Using expressions (20) of the mechanical strains and the approximation (17) of the displacement vector, we obtain a relationship between the stain vector ε Eq. (9) and the nodal degrees of freedom vector U_n Eq. (19):

$$\underset{6\times 120}{\left[B\right]}=\left[\begin{array}{l}\{N_{u,x}\}^T \\ \{N_{v,y}\}^T \\ \{N_{w,z}\}^T \\ \{N_{u,y}\}^T+\{N_{v,x}\}^T \\ \{N_{u,z}\}^T+\{N_{w,x}\}^T \\ \{N_{v,z}\}^T+\{N_{w,y}\}^T\end{array}\right] \tag{21}$$

where:

$$\begin{aligned} N_{\alpha,x} &= j_{11}N_{\alpha,\xi}+j_{12}N_{\alpha,\eta}+j_{13}N_{\alpha,\zeta} \\ N_{\alpha,y} &= j_{21}N_{\alpha,\xi}+j_{22}N_{\alpha,\eta}+j_{23}N_{\alpha,\zeta} \quad ; \quad \alpha\equiv u,v,w \\ N_{\alpha,z} &= j_{31}N_{\alpha,\xi}+j_{32}N_{\alpha,\eta}+j_{33}N_{\alpha,\zeta} \end{aligned} \tag{22}$$

and j_{lk} are the Jacobian inverse matrix components $\left(\left[j\right]=\left[J\right]^{-1}\right)$, so the Jacobian matrix takes the following form:

$$\left[J\right]=\left[\begin{array}{ccc} x_{,\xi} & y_{,\xi} & z_{,\xi} \\ x_{,\eta} & y_{,\eta} & z_{,\eta} \\ x_{,\zeta} & y_{,\zeta} & z_{,\zeta}\end{array}\right] \tag{23}$$

Based on Eq. (8), (17) and (20), the virtual potential energy at the element level becomes:

$$W^e = \{\delta U_n\}^T \left[\underbrace{\int_{\Omega^e} [B]^T [H][B] d\Omega}_{[K^e]} \{U_n\} - \left(\underbrace{\int_{\Omega^e} [N]^T \{f^v\} d\Omega + \int_{\Gamma} [N]^T \{T\} dA}_{f^e_{ext}} \right) \right] \tag{24}$$

where $\left[K^e\right]$ is the element stiffness matrix in the global coordinate system, f^e_{ext} is the element external force vector and $\left[H\right]$ is the three dimensional elastic matrix written for a homogeneous and isotropic material:

$$[H] = \begin{bmatrix} 2G+\lambda & \lambda & \lambda & 0 & 0 & 0 \\ \lambda & 2G+\lambda & \lambda & 0 & 0 & 0 \\ \lambda & \lambda & 2G+\lambda & 0 & 0 & 0 \\ 0 & 0 & 0 & G & 0 & 0 \\ 0 & 0 & 0 & 0 & G & 0 \\ 0 & 0 & 0 & 0 & 0 & G \end{bmatrix} \tag{25}$$

The coefficients G and λ are expressed in terms of Young's modulus and Poisson's ratio:

$$\begin{cases} \lambda = \dfrac{E\nu}{(1+\nu)(1-2\nu)} \\ \\ G = \dfrac{E}{2(1+\nu)} \end{cases} \tag{26}$$

4 INCOMPATIBLE SPACE FIBER ROTATION ELEMENT

In this section we present the nonconforming element denoted SFR20I. The element uses a similar approach as given by Yunus et al. [23] and Ayad et al. [29] to avoid some shortcomings related to the Poisson locking phenomena. In this regard, three incompatible displacement modes at the element level are introduced in the natural space a_u , a_v and a_w . The natural space extra modes are given as follows:

$$\begin{cases} U^{NC} = \left(1-\xi^2\right) a_u \\ V^{NC} = \left(1-\eta^2\right) a_v \\ W^{NC} = \left(1-\zeta^2\right) a_w \end{cases} \tag{27}$$

where *NC* stands for Non-Conforming. Natural or covariant non-conforming strains are determined by:

$$\varepsilon^{NC}_{\xi\xi} = \frac{\partial U^{NC}}{\partial \xi} \quad ; \quad \varepsilon^{NC}_{\eta\eta} = \frac{\partial V^{NC}}{\partial \eta} \quad ; \varepsilon^{NC}_{\zeta\zeta} = \frac{\partial W^{NC}}{\partial \zeta} \quad ; \quad \gamma^{NC}_{\xi\eta} = \gamma^{NC}_{\xi\zeta} = \gamma^{NC}_{\eta\zeta} = 0 \tag{28}$$

and the vector of natural strains is related to the incompatible modes a_u , a_v and a_w through a matrix $\left[M\right]$ as:

$$\varepsilon^{NC}_{\xi} = [M]\{a\} \tag{29}$$

$$\begin{Bmatrix} \varepsilon_{\xi\xi}^{NC} \\ \varepsilon_{\eta\eta}^{NC} \\ \varepsilon_{\zeta\zeta}^{NC} \\ \gamma_{\xi\eta}^{NC} \\ \gamma_{\xi\zeta}^{NC} \\ \gamma_{\eta\zeta}^{NC} \end{Bmatrix} = \begin{bmatrix} -2\xi & 0 & 0 \\ 0 & -2\eta & 0 \\ 0 & 0 & -2\zeta \\ 0 & 0 & 0 \\ 0 & 0 & 0 \\ 0 & 0 & 0 \end{bmatrix} \begin{Bmatrix} a_u \\ a_v \\ a_w \end{Bmatrix} \tag{30}$$

To verify the orthogonality condition between constant stress and non-conforming strain vectors (ensuring the satisfaction of the patch test); we consider the following relationship between Cartesian and natural non-conforming strains:

$$\left\{\varepsilon_X^{NC}\right\} = \frac{detJ_0}{detJ}\left[T_0\right]\left\{\varepsilon_\xi^{NC}\right\} = \frac{detJ_0}{detJ}\left[T_0\right]\left[M\right]\left\{a\right\} \tag{31}$$

$$\left[M^{NC}\right] = \frac{detJ_0}{detJ}\left[T_0\right]\left[M\right] \tag{32}$$

where $\left[T_0\right]$ is the matrix relating Cartesian and covariant strain vectors evaluated at the element center and $detJ$ is the determinant of the Jacobian ($detJ_0$ is evaluated at the center of the element). The introduction of incompatible modes conduces to an enhanced strain vector:

$$\left\{\varepsilon^E\right\} = \left\{\varepsilon\right\} + \left\{\varepsilon^{NC}\right\} = \left[B\right]\left\{U_n\right\} + \left[M^{NC}\right]\left\{a\right\} \tag{33}$$

By replacing the new incompatible strain vector $\left\{\varepsilon^E\right\}$ in the equilibrium weak form Eq. (5), we obtain the following system of equations:

$$\begin{bmatrix} \left[K_{uu}^e\right] & \left[K_{ua}^e\right] \\ \left[K_{au}^e\right] & \left[K_{aa}^e\right] \end{bmatrix} \begin{Bmatrix} \left\{U_n\right\} \\ \left\{a\right\} \end{Bmatrix} = \begin{Bmatrix} \left\{f_{ext}^e\right\} \\ 0 \end{Bmatrix} \tag{34}$$

$$\left[K_{uu}^e\right] = \int_{\Omega^e} \left[B\right]^T \left[H\right]\left[B\right] d\Omega \tag{35}$$

$$\left[K_{ua}^e\right] = \int_{\Omega^e} \left[B\right]^T \left[H\right]\left[M^{NC}\right] d\Omega \tag{36}$$

$$\left[K_{au}^e\right] = \left[K_{ua}^e\right]^T \tag{37}$$

$$\left[K_{aa}^e\right] = \int_{\Omega^e} \left[M^{NC}\right]^T \left[H\right]\left[M^{NC}\right] d\Omega \tag{38}$$

Static condensation of the tangent matrix is performed to eliminate the unknown enhanced parameters $\left\{a\right\}$ at element level. And, the final element stiffness matrix of the non-conforming element SFR20I is given as:

$$\left[K^e\right] = \left[K_{uu}^e\right] - \left[K_{ua}^e\right]\left[K_{aa}^e\right]^{-1}\left[K_{au}^e\right] \tag{39}$$

5 NUMERICAL INTEGRATION SCHEMES

The Gaussian integration on the reference element is necessary to obtain the element stiffness matrix in a standard formulation based on displacement, so the element stiffness matrix is expressed in the parametric reference $\left(\xi,\eta,\zeta\right)$ as the following form:

$$\begin{aligned}\left[K^{e}\right] &= \int_{\Omega^{e}}\left[B\right]^{T}\left[H\right]\left[B\right]d\Omega^{e} = \int_{-1}^{1}\int_{-1}^{1}\int_{-1}^{1}\left(\left[B\right]^{T}\left[H\right]\left[B\right]DetJ\right)_{\xi,\eta,\zeta} d\xi d\eta d\zeta \\ \left[K^{e}\right] &= \sum_{i=1}^{m}\sum_{j=1}^{m}\sum_{k=1}^{m} w_{i}w_{j}w_{k}\left(\left[B\right]^{T}\left[H\right]\left[B\right]DetJ\right)_{\xi,\eta,\zeta}\end{aligned} \tag{40}$$

where $DetJ$ is the Jacobian determinant taken at Gauss points of the transformation between the unit configuration and the parametric reference. A $\left(3\times3\times3\right)$ Gauss points scheme is needed to exactly determine the stiffness matrix part corresponding to the displacement DOFs while a $\left(4\times4\times4\right)$ Gauss points scheme is necessary to exactly assess the second part associated with the rotational DOFs. To render the elements SFR20 and SFR20I computationally more effective, we choose to adopt the reduced integration scheme with $\left(3\times3\times3\right)$ Gauss points to assess the elementary stiffness matrix $\left[K_{uu}^{e}\right]$ (the reduced integration concerns only the part related to rotational DOFs).

6 NUMERICAL VALIDATION

In this section, the performance and efficiency of the proposed elements are evaluated through a series of 3D benchmarks. In this context, the obtained results are compared with the analytical solution on the one hand and with those of other reference elements Table 1 on the other hand. Computations are performed using the finite element code Reflex developed by Batoz and Dhatt [41].

Table 1
Listing of abbreviations to denote the element types.

Element name	Description
HEX20	20-node hexahedral standard element tested by MacNeal and Harder [3];
HEX20(R)	20-node hexahedral standard element with reduced integration tested by MacNeal and Harder in [3];
SHB20	20-node solid-shell element [42];
C3D20	20-node second-order classical hexahedral Abaqus element with an exact numerical integration scheme ($3\times3\times3$ Gauss points) [43];
C3D20R	20-node second-order classical hexahedral Abaqus element with reduced numerical integration scheme ($2\times2\times2$ Gauss points) [43];
SOLID95	20-node element of ANSYS 5.4 [44];
HEXA20	20-node isoparametric hexahedron classical symmetric element [38];
US-HEXA20	20-node Unsymmetric hexahedral element [38];
H27	27-node Lagrange element [45, 46];
HS21	21-node hexahedral spline element [40];
SFR20	Presented 20-node hexahedral element based upon the "Space Fiber Rotation" concept;
SFR20I	Presented 20-node hexahedral element based upon the "Space Fiber Rotation" concept with incompatible modes.

6.1 Maximum aspect ratio test

This test was examined in the works of Legay and Combescure [47] and Abed Meraim et al. [42] to evaluate the aspect ratio limits of elements in beam bending problems. It consists of a clamped beam subjected to a bending load at its free edge as depicted in Fig. 3. The analytical solution of this problem can be obtained using the beam theory Eq. (41):

$$Y^{ref} = PL^3/3EI \quad ; \quad I = bt^3/12 \tag{41}$$

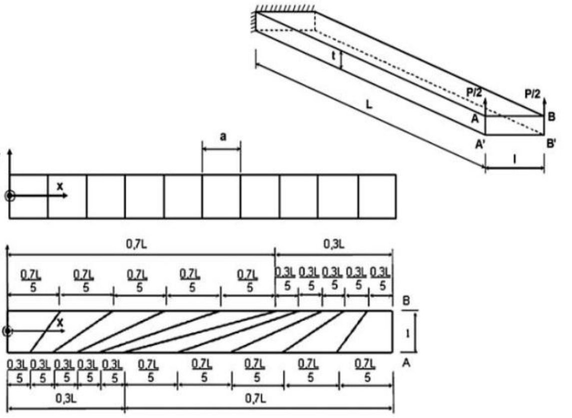

Fig.3
Cantilever beam geometry and mesh description.

The length and the width of the beam were constant and equal to $L = 100$ and $b = 10$, respectively. The beam was modeled with one element through the thickness and the width, in the length of the beam 10 elements were used in both regular and irregular meshes, the aspect ratio between the width and the thickness is $r = b/t$. The mechanical properties of the beam are: $E = 68.25 \times 10^6$ and $\nu = 0.3$. A bending load $P = 4$ is applied at the free end of the beam.

Table 2
Normalized displacement at point *A* for regular meshes.

Aspect ratio (*r* = *b/t*)	Ref. Solutions	HEX20	SHB20	SFR20	SFR20I
1	2.344E-5	1.005	1.009	0.993	1.005
10	2.344E-4	0.984	0.998	0.999	1.009
100	2.344E-3	0.951	0.997	1.001	1.010
200	4.689E-3	0.959	0.996	1.001	1.010
333	7.814E-3	NA	0.998	1.001	1.010
500	1.172E-2	NA	1.004	1.001	1.010

The results of the displacement at point A of different elements are shown in Tables 2 and 3 for both regular and distorted meshes. The findings of the proposed elements and the solid-shell element SHB20 are in good agreement with the analytical solution even when the thickness decreases. However, the standard hexahedron HEX20 loses accuracy when the aspect ratio increases especially for the distorted mesh. The normalized displacement for regular and distorted meshes are plotted against the aspect ratio evolution in Fig. 4 and 5 respectively.

Table 3
Normalized displacement at point *A* for irregular (distorted) meshes.

Aspect ratio (*r* = *b/t*)	Ref. Solutions	HEX20	SHB20	SFR20	SFR20I
1	2.344E-5	0.981	1.010	0.982	0.994
10	2.344E-4	0.682	0.997	0.988	0.998
100	2.344E-3	0.345	0.995	0.989	0.999
200	4.689E-3	0.294	1.002	0.989	0.999
333	7.814E-3	0.251	0.984	0.989	0.999
500	1.172E-2	NA	NA	0,989	0.999

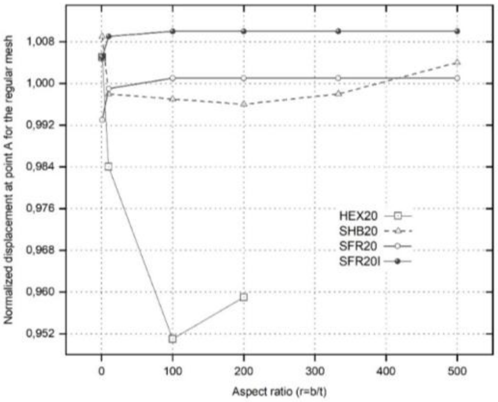

Fig.4
Convergence of normalized displacement at point *A* as a function of the aspect ration for regular mesh.

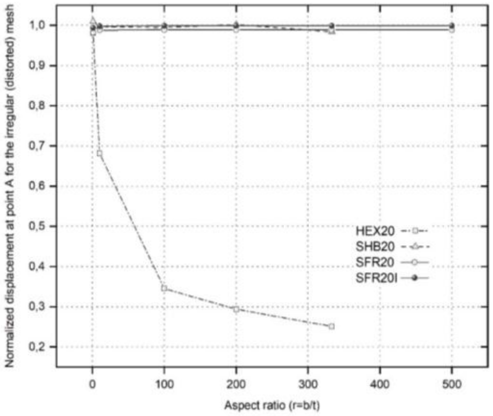

Fig.5
Convergence of normalized displacement at point *A* as a function of the aspect ration for irregular (distorted) mesh.

6.2 In-plane bending of a cantilever beam

As shown in Fig. 6, the second numerical example considers a cantilever beam subjected to in plane bending load $P_y = 1.0\times 10^4$. The beam is supposed to have the following physical properties: $E = 1.0\times 10^7$, $\nu = 0.3$. This cantilever beam is modeled with six meshes: three regular meshes : *M*1, *M*2 and *M*3 and three distorted ones : *M*4, *M*5 and, *M*6 as shown in Fig. 7. The reference solution of the transverse displacement at point C can be obtained using the Timoshenko beam theory Eq. (42):

$$W_C^{ref} = \frac{PL^3}{3EI} + \frac{6PL}{5GA} = 4 + 0.03 = 4.03 \tag{42}$$

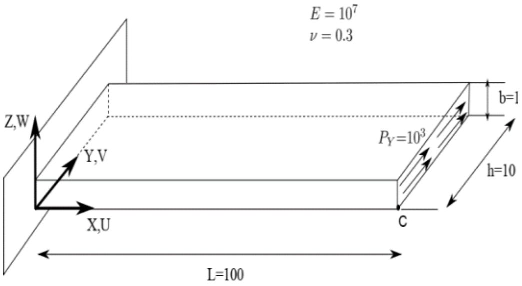

Fig.6
Geometry and mechanical properties of a thin cantilever beam under plane bending.

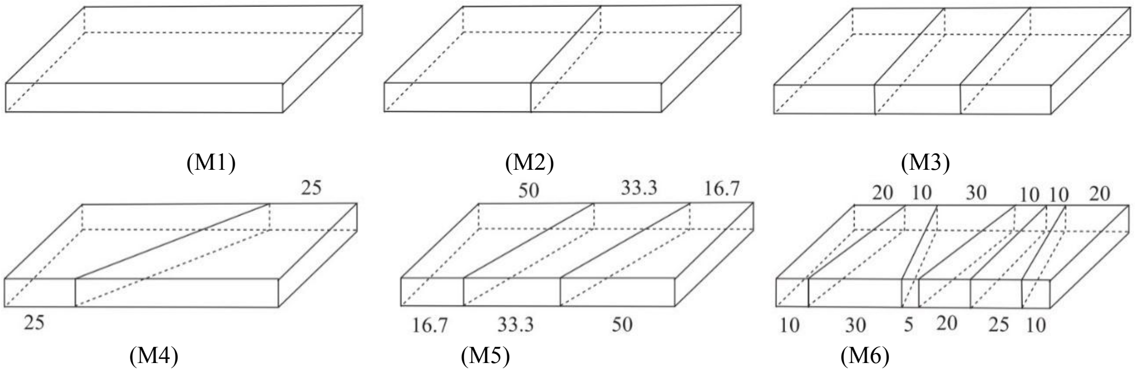

Fig.7
Mesh types of the thin cantilever beam.

The findings of different solutions are summarized in Table 4. This table compares the normalized displacement at point C of the proposed elements with the results of the quadratic hexahedral element of Abaqus C3D20. Both SFR20 and SFR20I show favorable behaviour and good rate of convergence. Especialy, in the distorted mesh unlike the element C3D20.

Table 4
In-plane bending of a cantilever beam. Normalized transverse displacement of point *C* (the value inside parentheses indicates the total number of variables in the model: DOFs plus internal variables).

Mesh Shape	$M1$	$M2$	$M3$	$M4$	$M5$	$M6$
C3D20	0.735	0.899	0.972	0.146	0.424	0.859
	(60)	(96)	(132)	(96)	(132)	(240)
SFR20	0.966	0.977	0.981	0.887	0.948	0.988
	(120)	(192)	(264)	(192)	(264)	(480)
SFR20I	0.998	0.999	0.999	0.907	0.957	1.012
	(123)	(198)	(273)	(198)	(273)	(498)

6.3 Straight cantilever beam

To evaluate the proposed elements' performance in terms of sensitivity to mesh distortion, a straight cantilever beam is considered. This example was examined in the work of MacNeal and Harder to test the combination of different shapes with linearly varying strains [3]. In this respect, The beam is meshed with six elements with different shapes (regular bricks, trapezoidal and parallelogram-shaped) and subjected to an in-plane and out-of-plane unit-shear force at the free end as shown in Fig. 8. The dimensions of the problem and the physical properties are: $Length = 6.0$; $width = 0.2$; $depth = 0.1$; $mesh = 6\times1\times1$; $E = 1.0\times10^{7}$; $\nu = 0.3$. The theoretical solutions for the problem are $U^{ref} = 0.1081$ and $W^{ref} = 0.4321$ for the in-plane and out-of-plane load, respectively.

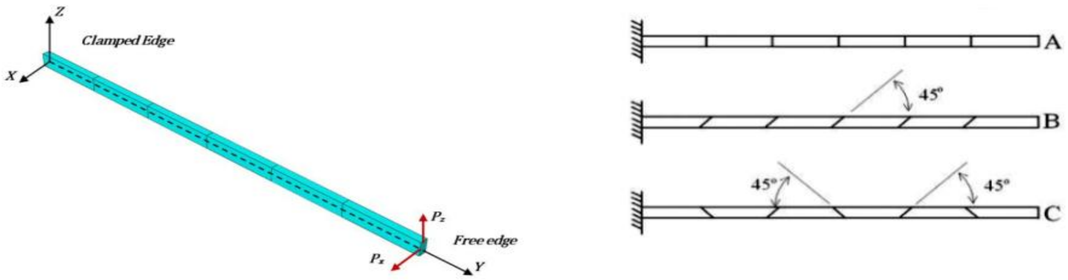

Fig.8
Straight cantilever beam with three types of meshes. A, rectangular; B, parallelogram; C, trapezoidal.

Table 5
Normalized tip deflection of a straight cantilever beam.

Element shape	Load type	HEX20	HEX20(R)	SOLID95	USHEXA20	SFR20	SFR20I
Regular	In-plane	0.970	0.984	0.994	0.994	0.990	0.998
	Out-of-plan	0.961	0.972	0.992	0.992	0.986	0.996
Trapezoidal	In-plane	0.886	0.964	0.966	0.985	0.989	0.995
	Out-of-plan	0.920	0.964	0.987	0.987	0.975	0.986
Parallelogram	In-plane	0.967	0.994	0.988	0.989	0.985	0.991
	Out-of-plan	0.941	0.961	0.987	0.987	0.946	0.964

Tables 5 compares the normalized tip deflection of the proposed elements with other reference elements. It can be noted that the SFR20 and SFR20I elements show good accuracy when trapezoidal shapes are used for both in-plane and out-of-plane loads. On the other hand, when parallelograms are used, the accuracy slightly diminishes when an out-of-plane load is applied.

6.4 Distortion tests

Fig. 9 demonstrates the geometry and boundary conditions of the Clamped beam presented in Areias et al. [48]. The mechanical properties are $E = 1500$ and $\nu = 0.25$. The beam is discretized using two sets of distorted mesh ($2\times1\times1$) and ($5\times1\times1$) elements for set-I and set-II respectively. Both sets are clamped and subjected to two cases of loading in the free end, a pure bending (case A) and a transverse/shear force (case B). The reference transverse displacement at point *C* for (case A) is $W_C^{ref} = 100$ while for (case B) is $W_C^{ref} = 102.6$. We summarize in Tables 6 and 7 the normalized transverse displacement of different solutions.

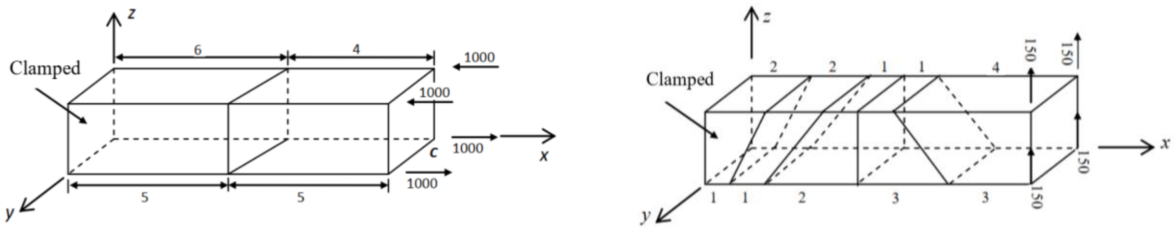

Distorted mesh set-I, loading case A.

Distorted mesh set-II, loading case B.

Fig.9
Clamped beam with distorted mesh.

For both sets, the presented elements exhibit good results. It can be noticed that the SFR20 element is slightly performant when compared with other solutions whereas the nonconforming SFR20I element is found to be more efficient in terms of convergence rate.

Table 6
Normalised transverse displacement of point *C* for set-I.

Case	SOLID95	USHEXA20	C3D20	H27	HS21	SFR20	SFR20I
A	0.999	1.000	0.962	0.998	1.003	0.981	1.000
B	0.978	0.978	0.924	0.958	0.939	0.968	0.992

Table 7
Normalised transverse displacement of point *C* for set-II.

Case	SOLID95	USHEXA20	C3D20	SFR20	SFR20I
A	0.997	1.000	0.982	0.999	1.004
B	1.005	1.011	0.975	0.995	1.091

6.5 Square clamped plate

This example is a popular benchmark to evaluate the performance and accuracy of finite elements [3, 38, 48]. Fig. 10 shows a square plate with clamped supports subjected to a point load of $P = 4\times10^{-4}$ at the center. The square plate of dimension $L = 2.0$ with uniform thickness $h = 0.01$ and material properties $E = 1.7472\times10^{7}$, $\nu = 0.3$. the convergence of the proposed elements was studied by modelling the square plate using one element through the thickness and N = 2, 4, 6, 8 and 10 elements on each side. The analytical solution for square clamped plate under a concentrated load is $W^{ref} = 5.6\times10^{-6}$. The normalized values of the deflection at the central point are given in Table 8.

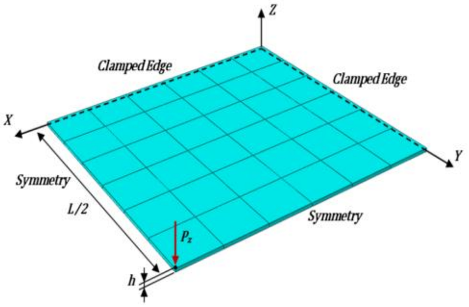

Fig.10
Square plate subjected to a concentrated load in the center with $4\times4\times1$ mesh.

From the observation of Fig. 11, it is clear that the best overall results are obtained with the presented elements and they converge rapidly to the exact solution. The rate of convergence is significant for a very coarse mesh $(N = 2)$ compared to the other quadratic hexahedral elements.

Table 8
Normalized transverse displacement at the center. Square plate with clamped supports subjected to a concentrated load.

Mesh	C3D20	C3D20R	SOLID95	HEXA20	USHEXA20	SFR20	SFR20I
2 × 2	NA	0.434	0.313	0.310	0.191	0.847	0.864
4 × 4	0.822	0.943	0.868	0.868	0.912	0.978	0.990
6 × 6	0.931	0.979	0.870	0.943	0.952	0.990	0.998
8 × 8	0.960	0.987	0.959	0.970	0.973	0.994	1.000
10 × 10	0.973	0.991	0.982	0.982	0.984	0.996	1.001

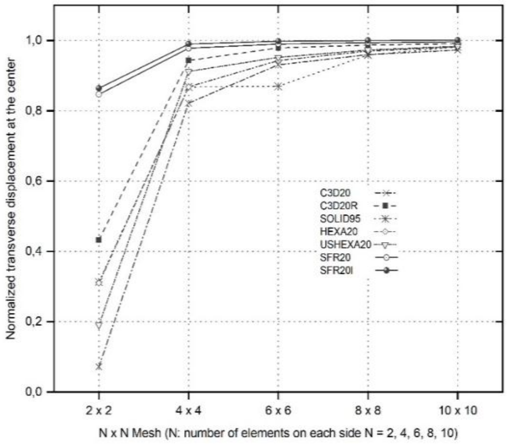

Fig.11
Convergence of normalized transverse displacement at the center. Square plate subjected to a concentrated load.

6.6 Circular plate

The test considers a circular plate clamped along the circumference and it is loaded with a concentrated force at the center. Because of the symmetry of the problem, only a quarter of the plate is discretized and the appropriate boundary conditions are applied on the symmetry plans. This quarter is modeled with one element through the thickness and N = 2, 4, 6, 8, 10 and 12 elements on each side. Geometry, mechanical properies and boundary conditions of the problem are indicated in Fig. 12. The analytical solution of the transverse displacement at the center is given by Kirchhoff plate theory [49] Eq. (43):

$$W^{ref} = \frac{3\left(1-\nu^{2}\right)FR^{2}}{4\pi Et^{3}} = 2.1725\times 10^{-3} \tag{43}$$

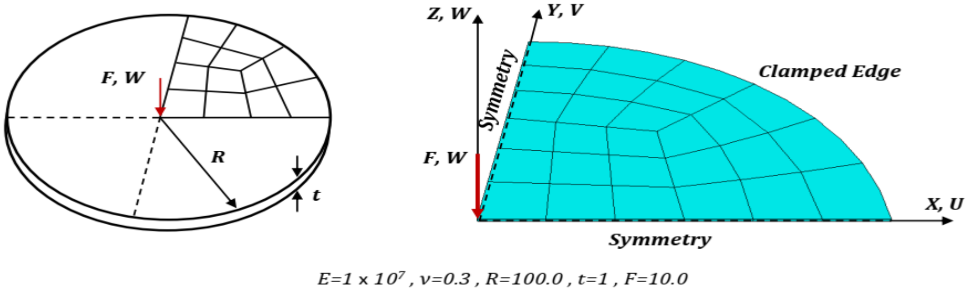

Fig.12
Problem statement of clamped circular plate under concentrated load.

Normalized values of different elements are presented in Tabel 9. It is clear that SFR20 and SFR20I present very accurate results when compared to the classical hexahedral element HEX20 and both Abaqus elements C3D20 and C3D20R. Besides, the presented elements are found to fastly converge to the analytical solution even with coarse mesh as shown in Fig. 13. Therefore, the SFR approach made adding another layer of elements across the thickness unnecessary.

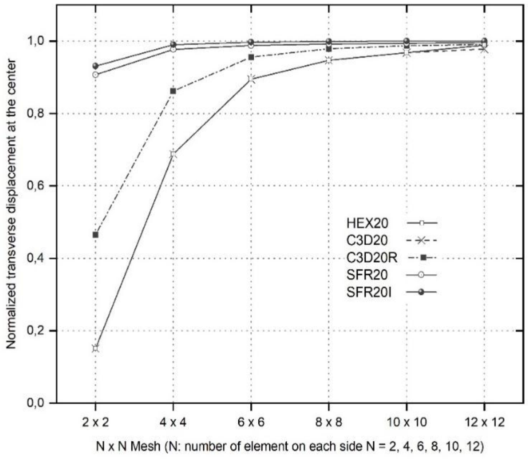

Fig.13
Convergence of nomalized transverse displacement at the center for circular plate problem.

Table 9
Normalized transverse displacement at the center. Circular plate with clamped supports subjected to a concentrated load.

Mesh	HEX20	C3D20	C3D20R	SFR20	SFR20I
2 × 2	0.151	0.151	0.465	0.907	0.931
4 × 4	0.688	0.688	0.863	0.977	0.990
6 × 6	0.895	0.895	0.956	0.988	0.997
8 × 8	0.947	0.947	0.979	0.992	0.999
10 × 10	0.968	0.968	0.987	0.994	1.000
12 × 12	0.989	0.978	0.991	0.996	1.000

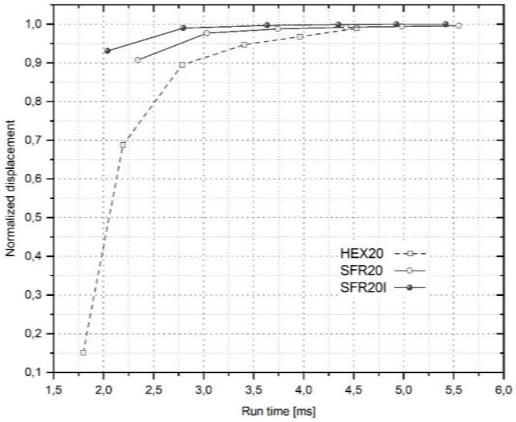

Fig.14
Computational cost for establishing the global stiffness matrix and the solving system equations of the circular plate problem.

In order to evaluate the run-time efficiency of the proposed elements, the computing time is now assessed for the circular plate problem analyzed above. The computational cost to set up the global stiffness matrix and to solve the algebraic equations is illustrated in Fig. 14. From the plots, we can conjecture that, for same displacement results, the run-time required for both SFR20 and SFR20I elements with the Space Fiber Rotation concept presented here appears asymptotically lower than that of the classical hexahedral element HEX20.

6.7 Pinched spherical shell

The following example deals with a hollow sphere with two radially opposed point loads as shown in Fig. 15. This example is usually used to check the absence of shear and membrane locking in structures exhibiting bending behavior. Dimensions, mechanical properties, and boundary conditions are shown in Table 10. Due to symmetry, only a quarter of the structure is discretized into $N \times N \times 1$ regular elements (N = 2, 4, 8 and 10 per side). The analytical solution of the problem is given in the paper of MacNeal and Harder [3]: $U_A = -V_B = 0.094$

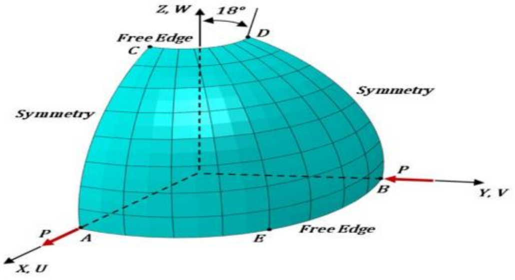

Fig.15
Hemisphere under diametrically opposite forces.

Table 10
Mechanical properties, geometry, boundary and symmetry conditions of shell tests.

	Pinched spherical shell	Pinched cylindrical shell with end diaphragms
Geometry and mechanical properties		
	$R=10,\ h=0.04,\ R/h=250,$	$L=6,\ R=3,\ h=0.03,$
	$E=6.825\times10^{7},\ \nu=0.3$	$E=3\times10^{10},\ \nu=0.3$
Boundary condition		
	$W=0\ on\ E$	$U=W=\theta_Y=0\ on\ AD$
Symmetry conditions		
	$V=\theta_X=\theta_Z=0\ on\ AC$	$W=\theta_X=\theta_Y=0\ on\ AB$
	$U=\theta_Y=\theta_Z=0\ on\ BD$	$V=\theta_X=\theta_Z=0\ on\ BC$
		$U=\theta_Y=\theta_Z=0\ on\ CD$
Load		
	$P=2$	$P_Z=-0.25$

Findings of displacements at point A of different solutions are summarized in Table 11. To evaluate the rate of convergence, the normalized displacements at point A are plotted against the number of elements in Fig. 16. The results show that the SFR20 and SFR20I elements are better than all reference elements in terms of accuracy and rate of convergence.

Table 11
Normalized tip displacement in the force direction for pinched spherical shell problem.

Mesh	C3D20	C320R	SOLID95	HEXA20	USHEXA20	SFR20	SFR20I
2 × 2	NA	0.203	NA	NA	NA	0.759	0.792
4 × 4	0.683	0.685	0.021433	0.021217	0.014711	0.994	1.015
8 × 8	0.984	0.988	0.258461	0.257849	0.611636	1.010	1.047
10 × 10	0.989	0.994	0.457268	0.456715	0.779302	1.010	1.052

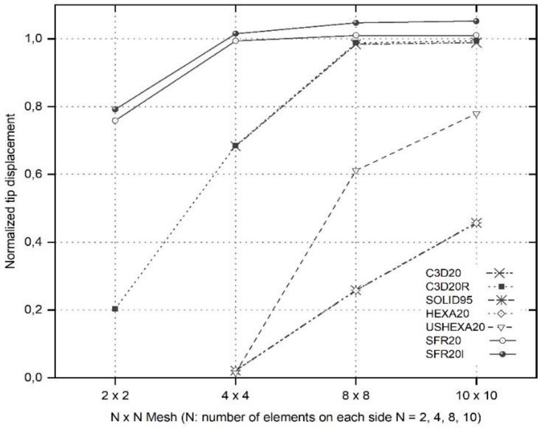

Fig.16
Convergence of normalized tip displacement of the pinched spherical shell.

6.8 Pinched cylindrical shell with end diaphragms

This last example considers a cylinder with rigid end diaphragms subjected to radially point load at point C, as shown in Fig. 17. This problem evaluates the performance of finite elements in both inextensional bending and complex membrane states of stress [50]. A reference solution of the present problem is given by Flügge [51] as:

$$W_C^{ref} = -\frac{W_C Eh}{P} = 164.24 \tag{44}$$

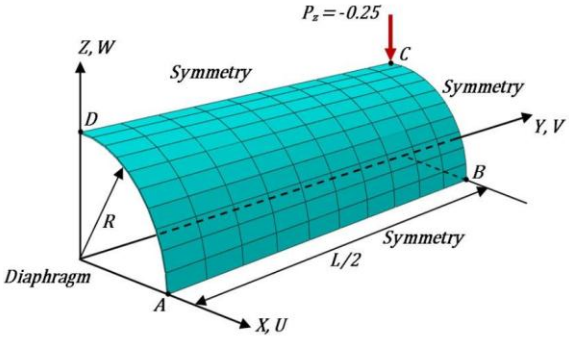

Fig.17
Pinched cylindrical shell with end diaphragms geometry, boundary and symmetry conditions; example of a $10\times10\times1$ mesh.

Dimensions, mechanical properties as well as applied boundary conditions are exposed in Table 10. The cylinder is modeled using a regular mesh of N = 2, 4 and 6 elements per side. Due to symmetry, only a segment of 90^o of the cylinder is examined with the appropriate boundary conditions along the symmetry plans. The displacements at point C of different element solutions are presented in Table 12.

Table 12
Normalised displacement for the pinched cylinder with diaphragms.

Mesh	HEX20	C3D20	C3D20R	SHB20	SFR20	SFR20I
2 × 2	NA	0.043	0.630	NA	0.468	0.551
4 × 4	0.140	0.140	0.872	0.883	0.823	0.932
6 × 6	0.328	0.328	0.952	0.961	0.929	1.057

The SFR20 give better results than the classical hexahedral element HEX20 and C3D20. We can notice a slight difference between the proposed element SFR20 and the elements C3D20R and SHB20. On the other hand, the findings of the non-conforming element SFR20I are much better than all the other counterparts.

7 CONCLUSION

This study set out to investigate the performance of two proposed 20-node hexahedral finite elements; a conforming element SFR20 and a non-conforming element SFR20I. These elements belong to the family of elements based on the Space Fiber Rotation concept. This formulation considers essentially a 3D rotation of a virtual fiber within the element which enriches the definition of the displacement field approximation. Therefore, this approach results in additional rotational DOFs per node. The incompatible modes approach was implemented into the non-conforming element SFR20I in order to overcome Poisson’s locking deficiency. The performance of the proposed elements is examined through popular benchmarks in which the efficiency is assessed by comparing the findings with analytical and numerical reference solutions. The presented elements exhibit good performance in terms of accuracy, rate of convergence, and sensitivity to mesh distortion. They are shown to be significantly better than the standard 20-node hexahedron. In particular, the SFR20I element showed excellent accuracy even for very coarse meshes. A natural progression of this work is to extend the formulation of these elements to account for geometric and material nonlinearities.

REFERENCES

[1] Babuska I., Aziz K., 1972, Survey lectures on the mathematical foundations of the finite element method, *The Mathematical Foundations of the Finite Element Method with Applications to Partial Differential Equations* **3**: 359.

[2] Musa S.M., 2012, *Computational Finite Element Methods in Nanotechnology*, CRC Press.

[3] Macneal R.H., Harder R.L., 1985, A proposed standard set of problems to test finite element accuracy, *Finite Elements in Analysis and Design* **1**(1): 3-20.

[4] Hughes T.J., Cohen M., Haroun M., 1978, Reduced and selective integration techniques in the finite element analysis of plates, *Nuclear Engineering and Design* **46**(1): 203-222.

[5] Zienkiewicz O.C., Taylor R.L., Too J., 1971, Reduced integration technique in general analysis of plates and shells, *International Journal for Numerical Methods in Engineering* **3**(2): 275-290.

[6] Wilson E.L., Taylor R.L., Doherty W.P., Ghaboussi J., 1973, Incompatible displacement models, *Numerical and Computer Methods in Structural Mechanics*, Academic Press.

[7] Taylor R.L., Beresford P.J., Wilson E.L., 1976, A non-conforming element for stress analysis, *International Journal for Numerical Methods in Engineering* **10**(6): 1211-1219.

[8] Simo J.C., Rifai M., 1990, A class of mixed assumed strain methods and the method of incompatible modes, *International Journal for Numerical Methods in Engineering* **29**(8): 1595-1638.

[9] Andelfinger U., Ramm E., 1993, EAS-elements for two-dimensional, three-dimensional, plate and shell structures and their equivalence to HR-elements, *International Journal for Numerical Methods in Engineering* **36**(8): 1311-1337.

[10] Simo J.C., Armero F., 1992, Geometrically non-linear enhanced strain mixed methods and the method of incompatible modes, *International Journal for Numerical Methods in Engineering* **33**(7): 1413-1449.

[11] Simo J.C., Armero F., Taylor R., 1993, Improved versions of assumed enhanced strain tri-linear elements for 3D finite deformation problems, *Computer Methods in Applied Mechanics and Engineering* **110**(3-4): 359-386.

[12] Fredriksson M., Ottosen N.S., 2007, Accurate eight-node hexahedral element, *International Journal for Numerical Methods in Engineering* **72**(6): 631-657.

[13] De Sousa R.A., Jorge R.N., Valente R.F., De Sá J.C., 2003, A new volumetric and shear locking-free 3D enhanced strain element, *Engineering Computations* **20**: 896-925.

[14] Pian T.H., 1995, State-of-the-art development of hybrid/mixed finite element method, *Finite Elements in Analysis and Design* **21**(1-2): 5-20.

[15] Pian T.H.H., 1978, A historical note about 'hybrid elements', *International Journal for Numerical Methods in Engineering* **12**(5): 891-892.

[16] Pian T.H., Sumihara K., 1984, Rational approach for assumed stress finite elements, *International Journal for Numerical Methods in Engineering* **20**(9): 1685-1695.

[17] Pian T.H., Tong P., 1986, Relations between incompatible displacement model and hybrid stress model, *International Journal for Numerical Methods in Engineering* **22**(1): 173-181.

[18] Sze K.Y., Ghali A., 1993, Hybrid hexahedral element for solids, plates, shells and beams by selective scaling, *International Journal for Numerical Methods in Engineering* **36**(9): 1519-1540.

[19] Bussamra F.L., Pimenta P.D.M., Freitas J.A.T.D., 2001, Hybrid-Trefftz stress elements for three-dimensional elastoplasticity, *Computer Assisted Mechanics and Engineering Sciences* **8**(2-3): 235-246.

[20] Bussamra F.L.S., Neto E.L., Raimundo Jr D.S., 2012, Hybrid quasi-Trefftz 3-D finite elements for laminated composite plates, *Computers & Structures* **92**: 185-192.

[21] Allman D., 1984, A compatible triangular element including vertex rotations for plane elasticity analysis, *Computers & Structures* **19**(1-2): 1-8.

[22] Yunus S.M., Saigal S., Cook R.D., 1989, On improved hybrid finite elements with rotational degrees of freedom, *International Journal for Numerical Methods in Engineering* **28**(4): 785-800.

[23] Yunus S.M., Pawlak T.P., Cook R.D., 1991, Solid elements with rotational degrees of freedom: Part 1-hexahedron elements, *International Journal for Numerical Methods in Engineering* **31**(3): 573-592.

[24] Pawlak T.P., Yunus S.M., Cook R.D., 1991, Solid elements with rotational degrees of freedom: Part II-tetrahedron elements, *International Journal for Numerical Methods in Engineering* **31**(3): 593-610.

[25] Ayad R., 2002, *Contribution à la Modélisation Numérique Pour l'Analyse des Solides et des Structures, et Pour la Mise en Forme des Fluides Non-Newtoniens, Application a des Matériaux d'emballage*, Habilitation to conduct researches, University of Reims, Reims, France.

[26] Shang Y., Li C.F., Jia K.Y., 2020, 8-node hexahedral unsymmetric element with rotation degrees of freedom for modified couple stress elasticity, *International Journal for Numerical Methods in Engineering* **121**(12): 2683-2700.

[27] Shang Y., Cen S., Zhou M.J., 2018, 8-node unsymmetric distortion-immune element based on Airy stress solutions for plane orthotropic problems, *Acta Mechanica* **229**(12): 5031-5049.

[28] Meftah K., Ayad R., Hecini M., 2013, A new 3D 6-node solid finite element based upon the "Space Fibre Rotation" concept, *European Journal of Computational Mechanics/Revue Européenne de Mécanique Numérique* **22**(1): 1-29.

[29] Ayad R., Zouari W., Meftah K., Zineb T. B., Benjeddou A., 2013, Enrichment of linear hexahedral finite elements using rotations of a virtual space fiber, *International Journal for Numerical Methods in Engineering* **95**(1): 46-70.

[30] Meftah K., Zouari W., Sedira L., Ayad R., 2016, Geometric non-linear hexahedral elements with rotational DOFs, *Computational Mechanics* **57**(1): 37-53.

[31] Meftah K., Sedira L., Zouari W., Ayad R., Hecini M., 2015, A multilayered 3D hexahedral finite element with rotational DOFs, *European Journal of Computational Mechanics* **24**(3): 107-128.

[32] Meftah K., Sedira L., 2019, A four-node tetrahedral finite element based on space fiber rotation concept, *Acta Universitatis Sapientiae, Electrical and Mechanical Engineering* **11**(1): 67-78.

[33] Ayadi A., Meftah K., Sedira L., Djahara H., 2019, An eight-node hexahedral finite element with rotational DOFs for elastoplastic applications, *Acta Universitatis Sapientiae, Electrical and Mechanical Engineering* **11**(1): 54-66.

[34] Ayadi A., Meftah K., Sedira L., 2020, Elastoplastic analysis of plane structures using improved membrane finite element with rotational DOFs: Elastoplastic analysis of plane structures, *Frattura ed Integrità Strutturale* **14**(52): 148-162.

[35] Zhang H., Kuang J.S., 2008, Eight-node membrane element with drilling degrees of freedom for analysis of in-plane stiffness of thick floor plates, *International Journal for Numerical Methods in Engineering* **76**(13): 2117-2136.

[36] Madeo A., Casciaro R., Zagari G., Zinno R., Zucco G., 2014, A mixed isostatic 16 dof quadrilateral membrane element with drilling rotations, based on Airy stresses, *Finite Elements in Analysis and Design* **89**: 52-66.

[37] Nodargi N. A., Bisegna, P., 2017, A novel high-performance mixed membrane finite element for the analysis of inelastic structures, *Computers & Structures* **182**: 337-353.

[38] Ooi E.T., Rajendran S., Yeo J.H., 2004, A 20-node hexahedron element with enhanced distortion tolerance, *International Journal for Numerical Methods in Engineering* **60**(15): 2501-2530.

[39] Ooi E.T., Rajendran S., Yeo, J.H., 2007, Extension of unsymmetric finite elements US-QUAD8 and US-HEXA20 for geometric nonlinear analyses, *Engineering Computations* **24**: 407-431.

[40] Li C.J., Chen J., Chen W.J., 2011, A 3D hexahedral spline element, *Computers & Structures* **89**(23-24): 2303-2308.

[41] Batoz J.L., Dhatt G., 1990, *Modélisation des Structures par Eléments Finis : Solides Elastiques*, Presses Université Laval.

[42] Abed-Meraim F., Trinh V.D., Combescure A., 2013, New quadratic solid–shell elements and their evaluation on linear benchmark problems, *Computing* **95**(5): 373-394.

[43] ABAQUS, 2010, Analysis User's Manual, V.6.11.

[44] Kohnke P., 1997, *ANSYS: Theory Reference Release 5.4. ANSYS*, Inc: Canonsburg, PA.

[45] Bathe K.J., 2006, *Finite Element Procedures*, Klaus-Jurgen Bathe.

[46] Zienkiewicz O.C., Taylor R.L., Nithiarasu P., Zhu J.Z., 1977, *The Finite Element Method* , London, McGraw-Hill.

[47] Legay A., Combescure A., 2003, Elastoplastic stability analysis of shells using the physically stabilized finite element SHB8PS, *International Journal for Numerical Methods in Engineering* **57**(9): 1299-1322.

[48] Areias P.M.A., César de Sá J.M.A., António C.C., Fernandes A.A., 2003, Analysis of 3D problems using a new enhanced strain hexahedral element, *International Journal for Numerical Methods in Engineering* **58**(11): 1637-1682.

[49] Timoshenko S., Woinowsky-Krieger S., 1959, *Theory of Plates and Shells*, McGraw-Hill.

[50] Rabczuk T., Areias P.M.A., Belytschko T., 2007, A meshfree thin shell method for non-linear dynamic fracture, *International Journal for Numerical Methods in Engineering* **72**(5): 524-548.

[51] Flügge W., 2013, *Stresses in Shells*, Springer Science & Business Media.